Rainwater path in warm clouds derived from combined visible/near-infrared and microwave satellite observations

Ralf Bennartz,[1,2] Philip Watts,[2] Jan Fokke Meirink,[3] and Rob Roebeling[3]

Received 9 December 2009; revised 11 May 2010; accepted 15 June 2010; published 12 October 2010.

[1] The effects of warm rain on optical properties of clouds in the visible/near-infrared (VNIR) and passive microwave (PMW) are studied using a simple conceptual cloud model. It is shown that the combined use of PMW and VNIR observations allows for the detection of precipitation and the derivation of rainwater path utilizing the different physical information content of the two observation types. Various potential error sources are studied and one month of combined geostationary visible/near infrared and Advanced Microwave Scanning Radiometer-EOS (AMSR-E) passive microwave observations off the coast of South Africa are evaluated using the proposed approach. Comparisons with CloudSat radar reflectivities are used for an independent assessment. A gradual increase in retrieved rainwater path with column maximum radar reflectivity is found for reflectivity values larger than −10 dBz. For monthly mean values at 1 × 1 degree resolution, rainwater path is correlated with in-cloud liquid water path (R^2 = 0.50). The strongest correlation (R^2 = 0.69) exists between rainwater path and the inverse of cloud droplet number concentration (N). This finding is consistent with other studies supporting a 1/N dependency of precipitation intensity on cloud droplet number concentration in warm clouds.

Citation: Bennartz, R., P. Watts, J. F. Meirink, and R. Roebeling (2010), Rainwater path in warm clouds derived from combined visible/near-infrared and microwave satellite observations, *J. Geophys. Res.*, *115*, D19120, doi:10.1029/2009JD013679.

1. Introduction

[2] This paper explores the physical basis for the retrieval of precipitation amount from satellite-based observations of warm rain in the visible and near-infrared (VNIR) and microwave spectral range. VNIR observations of clouds provide two main pieces of information, the effective cloud droplet radius and optical thickness. These quantities can be retrieved from the combination of at least two measurements with and without liquid water absorption [*Nakajima and King*, 1990]. Various satellite instruments routinely provide measurements in these spectral bands and the derived quantities have become a major tool also in climate research, especially in the context of indirect aerosol effect studies. Retrieval algorithms are typically tailored toward non-precipitating clouds, assuming that the radiative signal of precipitation is small.

[3] Passive microwave (PMW) observations allow estimation of the column attenuation and, with additional assumptions, total liquid water path (TWP) and rain rate at the surface. The calculation of rain rate from PMW typically includes the separation of rainwater path (RWP) from cloud liquid water path (LWP) and requires assumptions about the height of the observed precipitation column, the raindroplet size distribution, and the partitioning between cloud liquid water and rainwater. Some algorithms specify the assumptions made in this separation explicitly [*Petty*, 1994a, 1994b; *Wentz and Spencer*, 1998] while other algorithms use lookup table approaches to derive rain rates consistent with PMW observations based largely on the output of mesoscale models [e.g., *Kummerow, et al.*, 2001]. For those algorithms the aforementioned partitioning is implicitly done in what has been termed the "cloud radiation database." While for meteorological applications the accuracy of these assumptions in the separation of RWP and LWP might not be of high significance, long-term climate records require a higher degree of accuracy and in particular require detailed knowledge about the correlative factors that might affect retrievals. These input parameters are critical for the retrieval of LWP [*O'Dell et al.*, 2008] and are often tuned so that the precipitation climatologies retrieved from PMW instruments resemble radar and/or rain gauge climatologies.

[4] Recently, a large number of papers have studied the differences in liquid water path retrieval based on PMW and VNIR observations [*Bennartz*, 2007; *Borg and Bennartz*, 2007; *Greenwald*, 2009; *Greenwald et al.*, 2007; *Horvath and Davies*, 2007; *Seethala and Horvath*, 2010; *Wilcox et al.*, 2009]. Differences between the two methods have been shown to be correlated with various factors, including cloud fraction, observation geometry, retrieval assumptions,

[1]Atmospheric and Oceanic Sciences, University of Wisconsin-Madison, Madison, Wisconsin, USA.
[2]EUMETSAT, Darmstadt, Germany.
[3]KNMI, De Bilt, Netherlands.

0148-0227/10/2009JD013679

aerosol above clouds, and others. No clear picture has yet emerged. This is partly caused by the correlative nature of the satellite studies, which does not necessarily allow causal relations to be established. A few issues are relatively clear. A slight (mostly) positive bias of Advanced Microwave Scanning Radiometer-EOS (AMSR-E) derived LWP in cloud-free situations in the order of 10 g/m^2 exists, which is cross-correlated with other AMSR-E retrieved variables [*Greenwald et al.*, 2007]. Also, the agreement between PMW and VNIR LWP estimates appears better for more stratiform clouds, where a near-adiabatic cloud liquid water profile can be assumed.

[5] Another line of research attempts to establish relations between observed precipitation rates and VNIR observations based on, e.g., collocated aircraft observation. *Roebeling and Holleman* [2009] combine information on liquid water path, particle effective radius, cloud thermodynamic phase, and cloud top temperature to detect precipitating clouds and retrieve rain rates from VNIR and IR observations. In addition, various publications use combinations of cloud droplet number concentration and liquid water path derived from VNIR to establish drizzle rates for stratocumulus cloud fields [e.g., *Bennartz*, 2007; *Comstock et al.*, 2004; *Geoffroy et al.*, 2008; *Pawlowska and Brenguier*, 2003; *van Zanten et al.*, 2005]. These findings are by definition correlative but are supported by scaling arguments for precipitation generation in warm clouds [*Kostinski*, 2008]. *Shao and Liu* [2004] use combined to PMW and VNIR observations to detect drizzle via a drizzle index.

[6] The current paper attempts to contribute to the aforementioned scientific discussions, but starts from a different point of view. We wish to study the radiative impact of precipitation on both the PMW and VNIR observations starting with a dynamically highly simplified but physically realistic conceptual cloud model. Various of the physical processes in this model are similar to the those proposed in *Wood et al.* [2009] although the model presented here is not steady-state. This model allows us to derive realistic profiles of cloud liquid water and precipitation within and underneath the cloud. Output of this model is used to study the radiative characteristics of the precipitating clouds. On the basis of the simulation results we propose the use of combined PMW and VNIR observations to derive rainwater path in warm, shallow clouds with some caveats. While the main thrust of this paper is theoretical, the approach is exemplarily applied to a combination of AMSR-E and Spinning Enhanced Visible and Infrared Imager (SEVIRI) data for four weeks of observations of the stratocumulus areas off the coast of southern Africa and CloudSat radar observations are used as an initial mechanism to evaluate the results against independent observations.

[7] The paper is organized in the following way. In section 2 the conceptual cloud model is briefly introduced (a more detailed description is deferred to Appendix A) and its general physical consistency is checked against aircraft observations. The raditiave transfer model and assumptions used are described in section 3. Section 4 evaluates the conceptual cloud model's VNIR and PMW response to precipitation in detail for the case of a stratiform cloud and explains the approach to derive RWP. Observational data are described in section 5 and the approach is tested using AMSR-E, SEVIRI, and CloudSat data in section 6. Conclusions are presented in section 7.

2. Conceptual Cloud Model

2.1. Model Description

[8] In order to study the impact of precipitation a conceptual one-dimensional cloud model has been developed. The model is described in detail in Appendix A. It can be thought of as a parcel model in which air is rising from the surface to the cloud top with a constant updraft velocity. The cloud base and maximum cloud geometrical thickness are specified beforehand. After the cloud top has been reached, the updraft velocity is set to zero and the cloud undergoes modifications only through entrainment at cloud top and precipitation production. If these processes are also switched off, the cloud remains adiabatic indefinitely. This model does include warm rain cloud microphysical processes, but accounts for dynamics only in a crude sense by specifying cloud base, cloud top, an updraft velocity, and an entrainment velocity at cloud top. In particular, the feedback between cloud microphysics and the dynamic state of the boundary layer, evaporation of raindroplets, and collisions between raindroplets are ignored. Therefore, the model cannot be used to study the behavior and temporal evolution of the cloud topped boundary layer in a fully quantitative sense. It does however provide some guidance on the vertical profiles of cloud water and rainwater content. This is supported by comparisons of model-generated precipitation rates generated with aircraft observations as shown below.

2.2. Model Evaluation and Comparison to Observed Cases

[9] We applied the conceptual model to various cases of stratiform clouds reported in the literature. In particular, we used the Second Dynamics and Chemistry of Marine Stratocumulus field study (DYCOMS-II [*Stevens et al.*, 2003]) cases reported by *van Zanten et al.* [2005] and various cases reported by *Wood* [2005a]. From the latter data set we ignored cases where multilayer clouds were reported. Input parameters to the model were the reported values of cloud droplet number concentration, condensation rate derived from cloud top temperature, and geometrical thickness. In each case the model was run until either the cloud liquid water vanished or for 4 h integration time, whichever occurred earlier. Figure 1 shows an example of the temporal evolution of the model for case 6 reported by *van Zanten et al.* [2005]. The profiles show the vertical distribution of rainwater and cloud liquid water at five different time steps. Between Profile 1 and Profile 3, liquid water is converted to rainwater in the middle part of the cloud, resulting in a significant subadiabaticity of the cloud profile. At the same time, entrainment from cloud top reduces cloud liquid water content in the uppermost part of the cloud. At later stages the cloud thins significantly because of ongoing precipitation production combined with entrainment mixing. It has to be noted again that this very simple cloud model is not meant to compete in any way with more complex and physically realistic models, such as Large Eddy Simulation (LES) tools. The model is simply used as a tool to create somewhat realistic rainwater and cloud liquid water profiles as input for radiative transfer calculation in

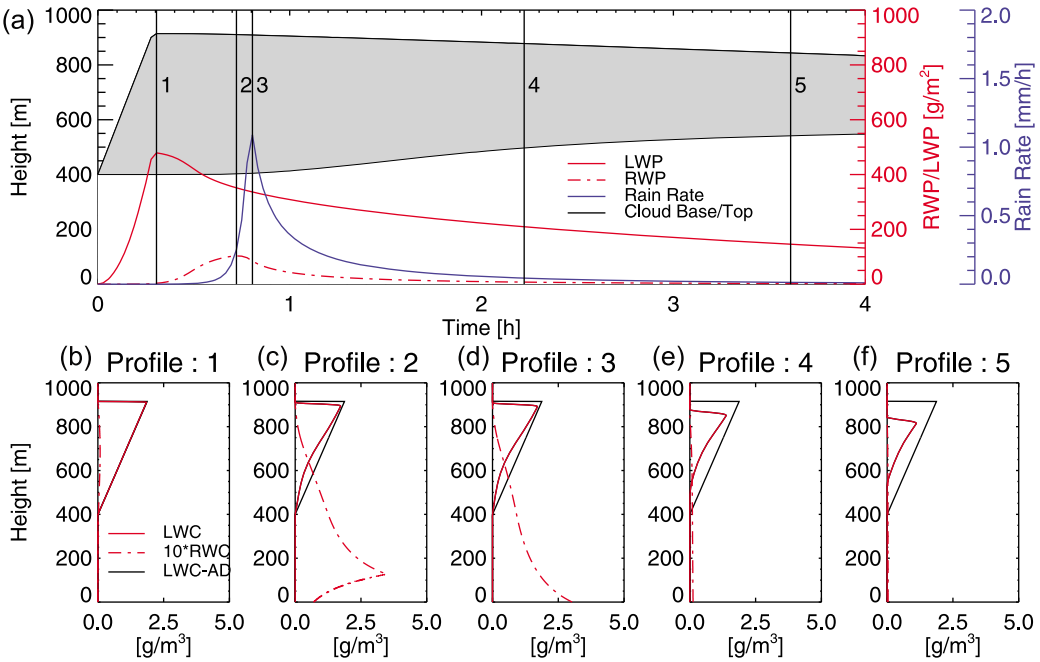

Figure 1. (a) Temporal evolution of the cloud geometrical thickness, liquid water path, rainwater path, and surface rain rate for the simulation of case 6 of the seven DYCOMS-II cases reported by *van Zanten et al.* [2005]. (b–f) Vertical profiles of liquid water content (LWC), rainwater content (RWC), and adiabatic liquid water content (LWC-AD) for the five times highlighted in Figure 1a. These times correspond to (1) the time of maximum LWP, (2) the time of maximum RWC, (3) the time of maximum surface rain rate, and (4 and 5) decaying stages of the cloud.

a conceptual study. Nevertheless, a partial validation of the model's precipitation generation can be performed by comparing the time-averaged rain rate created by the model to the values reported by *van Zanten et al.* [2005] and *Wood* [2005b]. A striking agreement between observed and simulated cloud base precipitation rates is found especially for the DYCOMS-II cases (Figure 2).

[10] The cases reported by *Wood* [2005a] are on average also reproduced, but the scatter is much larger than for the DYCOMS-II cases. This result is in agreement with *Wood* [2005a] who found a better linear agreement between the rain rates reported for DYCOMS-II and empirically derived fits of rain rate versus retrieved values of H^3/N. This quantity (H^3/N) can be derived from effective radius and optical thickness retrievals assuming an adiabatic cloud. On the basis of the studies by *Pawlowska and Brenguier* [2003] and *van Zanten et al.* [2005] it scales about linearly with cloud base precipitation rate for stratocumulus clouds. These results suggest a general consistency between the conceptual cloud model and a wide variety of different cases observed from aircraft experiments at least for precipitation generation.

3. Radiative Transfer Simulations

[11] Radiative transfer simulations were performed with a solar, azimuthally resolved version of the Successive Order of Interaction (SOI) radiative transfer model [*Heidinger et al.*, 2006; *O'Dell et al.*, 2006]. Subsequently, we discuss the cloud and raindroplet size distribution parameterization followed by assumptions specific to the VNIR and PMW spectral ranges.

3.1. Cloud and Raindroplet Size Distribution

[12] Cloud droplet size distributions are parameterized as a lognormal function depending on cloud liquid water content and cloud droplet number concentration. The width of the lognormal function was chosen so that relationship between the volume radius (r_v) and effective radius (r_e), expressed as, $k = r_3^v/r_e^3$, is conserved throughout the cloud at a value of k = 0.8 [see *Bennartz*, 2007; *Martin et al.*, 1994; *Pawlowska and Brenguier*, 2000]. This results in a relatively narrow size distribution for low liquid water content,

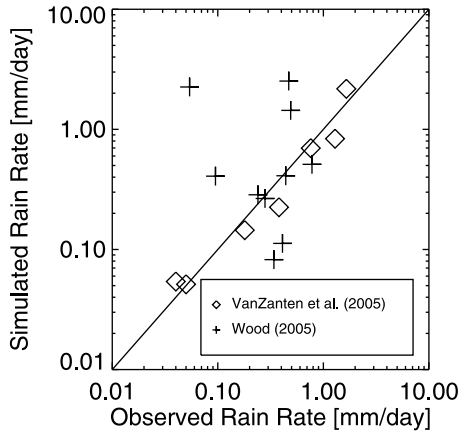

Figure 2. Comparison of simulated and observed averaged cloud base rain rates for the seven DYCOMS-II cases reported by *van Zanten et al.* [2005] and ten cases reported by *Wood* [2005a].

which widens somewhat for higher liquid water content. It yields somewhat wider spectra than those used in [*Schüller et al.*, 2003], which were purely based on adiabatic theory and were likely to underestimate the observed widening of the spectrum at higher liquid water content. The droplet spectra used here are insofar broadly in agreement with observations as k has been chosen to fall within this range. For the impact of differences in the choice of k, see the study by *Bennartz* [2007].

[13] Raindroplet spectra are simulated based on rainwater content and raindroplet number using the size distribution provided by *Wood* [2005b], which is based on observations and valid for drizzle. For higher rainwater contents it might be better to use a typical Marshall-Palmer size distribution. However, differences between them, in terms of PMW and VNIR optical properties, are small for rain rates smaller than 2–5 mm/h. Only for larger rain rates do differences become more substantial. Therefore, throughout this paper we keep the size distribution provided by *Wood* [2005b] in order to keep the simulations consistent.

3.2. Visible/Near-Infrared Modeling

[14] For the conceptual study azimuthally averaged radiances were calculated because of runtime constraints. VNIR Radiative transfer simulations were performed for the cloud only, ignoring Rayleigh and aerosol scattering, surface reflectance, and gaseous absorption. This is justified since the retrievals are only used in an idealized case study.

[15] Mie calculations and subsequent radiative transfer calculations were performed for in total five monochromatic channels at 639 nm, 808 nm, 1632 nm, 2130 nm, and 3891 nm, resembling typical channel positions for cloud retrievals for the Moderate Resolution Imaging Spectroradiometer (MODIS) onboard NASA's Terra and Aqua platform or the SEVIRI instrument onboard EUMETSAT's Meteosat Second Generation (MSG) geostationary platforms. The vertical resolution of 1 m provided by the conceptual cloud model was used also in the radiative transfer simulations.

[16] In order to allow for the evaluation of the results in retrieved cloud parameter space, a simple retrieval algorithm based on a nearest neighbor search within a lookup table was set up. For the retrievals performed on the simulated data, a large set of radiative transfer simulations was performed for adiabatic clouds with droplet number concentration N ranging from 1 cm^{-3} to 500 cm^{-3} in steps of 1 cm^{-3} and geometrical thickness H ranging from 5 m to 500 m in steps of 5 m. The retrieval of these values for a given simulated cloud reflectance was then performed using a nearest neighbor search in reflectance space. This simple and computationally inefficient search is not suited for operational retrievals but yields accurate results for the simulated cases investigated here. For the observational results provided further below we use as a retrieval the Cloud Physical Properties (CPP) retrievals of the EUMETSAT Satellite Application Facility on Climate Monitoring (CM-SAF). A detailed description of the CPP algorithm is given in section 5.1.

3.3. Passive Microwave Optical Properties

[17] For the PMW simulations we used the thermal version of the SOI model coupled with the FASTEM-2 surface emissivity model [*Deblonde and English*, 2001]. The temperature lapse rate within the boundary layer was set to follow dry adiabatic conditions outside the cloud and saturated adiabatic conditions within. In the free atmosphere the lapse rate was chosen to be slightly stable. Sea surface temperature was set so that the wind speed was held constant at 8 m/s. Water vapor was distributed in the atmosphere so that within the cloud, relative humidity reaches 100%. The total water vapor column amount was chosen to be 20 kg/m^2 (by adjusting the free troposphere water vapor). For water vapor and dry air absorption the model of *Rosenkranz* [1999] with recent modifications was used. Note that the particular choice of the atmospheric temperature and water vapor profile have virtually no impact on the considerations below, since the PMW response to cloud and rainwater is studied. For cloud liquid water absorption the [*Liebe et al.*, 1991] model with modifications by Rosenkranz was used. Rainwater extinction and scattering properties were calculated using Mie theory and the aforementioned size distribution of *Wood* [2005b] as well as Marshall-Palmer type size distributions for comparison.

4. Simulation Results for Precipitating Clouds

4.1. VNIR and PMW Response to Cloud and Rain

[18] Figure 3a shows bispectral reflectance plots for the model cloud shown in Figure 1 for the SEVIRI channel combinations used in cloud retrievals and the two main PMW frequencies carrying information about cloud liquid water (Figure 3b). For the VNIR channels, simulated reflectances are staying very close to the reflectance of an idealized adiabatic cloud (yellow curve) with maximum deviations only in the order of 1%. These deviations are not due to the direct precipitation signal but due to the combined effect of precipitation scavenging and entrainment changing the droplet size distribution over time. Differences between simulated reflectances with and without the optical properties of the precipitation are two orders of magnitude smaller (not shown). A direct signal of precipitation in VNIR observations therefore cannot be detected, if the cloud is sufficiently horizontally homogeneous and contains enough cloud liquid water. Figure 3c shows the same reflectances as a function of time, corresponding to Figure 1a. The saturation effect of the near-infrared channel becomes more apparent here, with the 1.6 μm channel's reflectance leveling out at values slightly above 40%. The 0.8 μm channel shows a somewhat larger variation and is essentially following changes in cloud liquid water path via optical depth.

[19] Very similar to the bispectral reflectance plots (Nakajima-King diagram) in Figure 3a, Figure 3b shows the PMW response for two microwave channels at 23.8 GHz and 36.5 GHz. Shown are the polarization differences for these two channels, which correspond most closely to changes in atmospheric transmittance. In a nonscattering atmosphere the polarization of PMW observations is caused solely by the polarized ocean surface, hence a reduction in polarization corresponds to an increase in atmospheric opacity. These two channels provide the main information content about LWP and water vapor path (WVP) for passive microwave retrievals. Strictly speaking, variations in surface wind speed would also affect the brightness temperature differences shown here, since it controls the degree of polarization

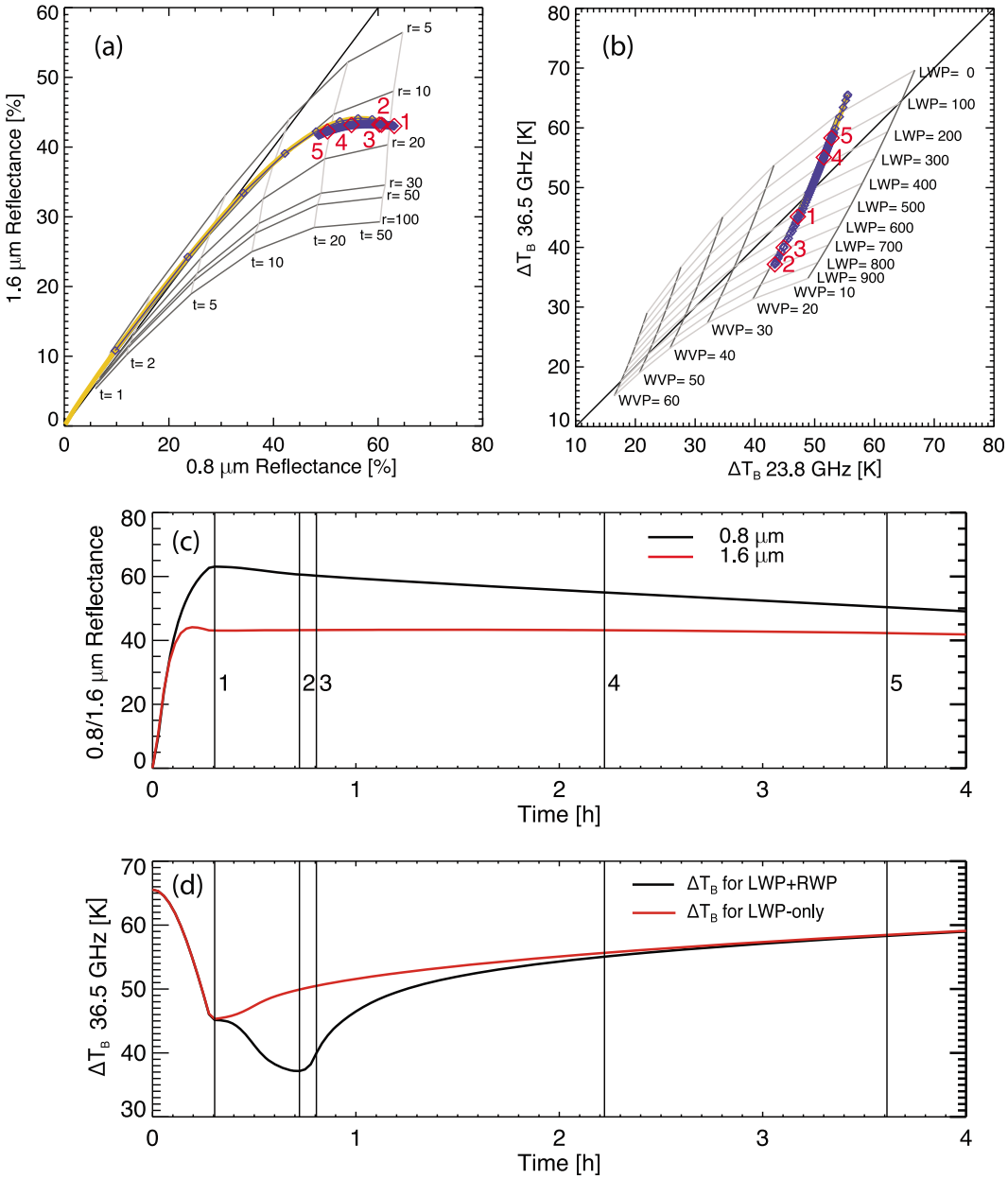

Figure 3. (a) A VNIR bispectral reflectance plot for clouds with different optical thickness/effective radius (following *Nakajima and King* [1990]). (b) Corresponding PMW polarization differences at 23.8 and 36.5 GHz. (c, d) The temporal evolution of the same data. The blue curve shows the trajectory of the stratiform cloud (Figure 1) in reflectance space (Figure 3a) and brightness temperature space (Figure 3b). The grids in Figure 3a show reflectance values for different combinations of effective radius (in μm, labeled r = 5…100) and optical thickness (labeled t = 1…50) for nadir observations and a solar zenith angle of 65 degrees. The grid in Figure 3b corresponds to water vapor path (WVP in kg/m^2) and LWP in g/m^2 (at 55 degrees zenith angle). The numbered red diamonds correspond to the profiles shown in Figure 1. The smaller blue dots are equidistant in time with a time interval of 25 s. The yellow curve shows the development of an idealized adiabatic cloud without entrainment or precipitation generation. For details on the simulations, see text.

of the ocean emissivity in the first place. However, both wind speed and WVP are of no concern for this study and, as outlined above, are held constant at 8 m/s and 20 kg/m^2, respectively.

[20] The main PMW signal of RWP and LWP is a reduction in polarization at 36.5 GHz between almost 70 K for the cloud-free atmosphere and about 35 K for the most opaque atmosphere. Note, that all observations collapse by default on the 20 kg/m^2 WVP line. While the different development stages of the cloud (points 1 through 5) can be discerned in Figure 3b the pure adiabatic (yellow) line cannot be identified because it falls underneath the blue

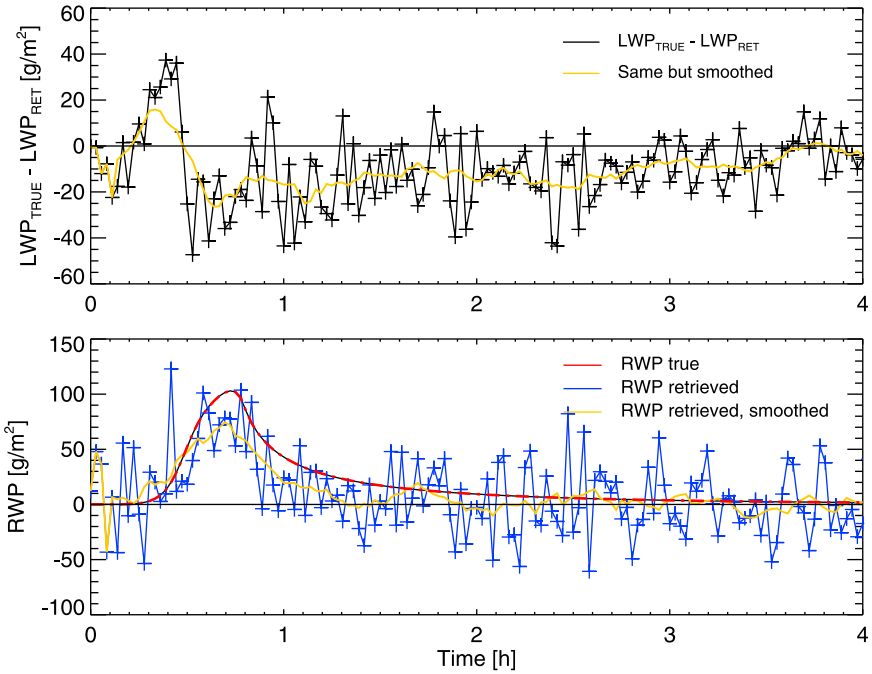

Figure 4. (top) Accuracy of a VNIR bispectral LWP retrieval for the stratiform cloud shown in Figure 1. Plotted are the differences between the actual cloud LWP (solid red line in Figure 1) and the retrieved cloud liquid water path. The yellow line shows the same data but smoothed over a time window of 10 time steps. (bottom) Actual RWP (red curve, corresponding to the dot-dashed red curve in Figure 1) and the retrieved RWP assuming the total water path is know from a PMW instrument (blue curve). The yellow curve is again smoothed over 10 time steps. All VNIR retrievals were performed with a signal-to-noise of 250, and the PMW retrieval noise was set to ±30 g/m^2.

curve for the actual cloud including cloud liquid water and rain. To understand the impact of rainwater versus cloud liquid water, it is therefore more revealing to study Figure 3d, where the two lines for the LWP-only cloud and the full simulation can be discerned easily when RWP is larger than zero. In fact, for the time corresponding to Profile 2 (maximum RWP), the additional depression in polarization difference because of RWP is in the order of 15 K (i.e., the maximum difference between the black and the red curve in Figure 3d). At that time the RWP is slightly above 100 g/m^2 and LWP is in the order of 380 g/m^2, (see Figure 1a). Note, that the sensitivities of the polarization difference to changes in LWP and RWP are slightly different. This is caused by differences in the mass extinction coefficient between rainwater and cloud water because of different droplet sizes, which is studied below in more detail. While cloud droplets are strictly within the Rayleigh regime, the larger raindroplets are entering the Mie regime causing increased absorption efficiencies and non-negligible scattering efficiencies as well. An important corollary of this dependency of extinction properties on droplet size is that TWP (and thus any subsequent separation into LWP and RWP) can only be inferred if an assumption about the droplet size distribution is made beforehand. Without this assumption a clear relation between the depolarization and TWP (or any other measure for column liquid water) cannot be inferred, since essentially the mass absorption coefficient is not known. A complete discussion of this issue and how it is accounted for in typical retrievals can be found in section 4.3 on RWP retrievals.

4.2. LWP From VNIR Observations

[21] Since the stratiform clouds discussed above do not produce a detectable direct VNIR radiative signal of precipitation, a retrieval of cloud LWP is possible for this type of cloud. Here we perform the LWP retrieval based on adiabatic theory as $LWP = 5/9\ \rho_L \tau r_e$ [*Wood and Hartmann*, 2006]. Figure 4 (top) shows the results of the aforementioned lookup table retrieval for the stratiform cloud. Recall that the retrieval is performed in N/H space for adiabatic clouds so that penetration depths of the different VNIR channel combinations are accounted for correctly within the retrieval itself. If a different retrieval approach based on vertically homogeneous clouds with fixed effective radii had been used, the different VNIR channel combinations would have yielded slightly different results based on penetration depth. This point speaks strongly for using N/H retrieval coordinate systems as pointed out by *Brenguier et al.* [2000].

[22] Between hours 0.5 and 3.5 Figure 4 (top) shows a slight overestimation of the retrieved LWP in the order of 20 g/m^2 or 5–10% of the total LWP. This results from the subadiabatic stratification of the precipitating clouds. Profile 3 in Figure 1 might serve as an example here. At heights of around 600 m as well as near cloud top the LWC profile is strongly subadiabatic. The actual geometrical extent of the cloud is 510 m at this time. The actual cloud LWP is 351.6 g/m^2. This LWP corresponds to an equivalent

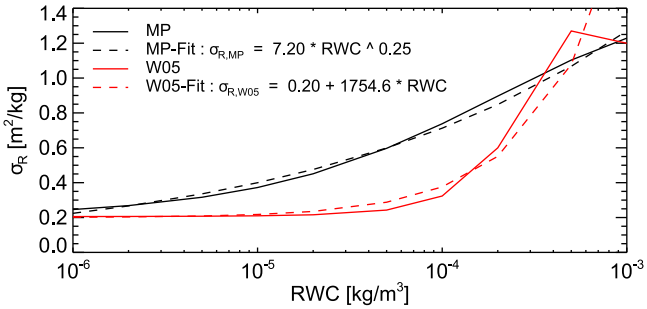

Figure 5. Mass absorption coefficient σ_R of liquid rain as a function of rainwater content. The black curve shows the mass absorption coefficient if a Marshall-Palmer size distribution is assumed (MP). The red curve assumes a size distribution according to *Wood* [2005b] (W05). The dashed lines provide fits to the solid curves with fit parameter and all units as given in the legend and all units as given in the axes labels (SI).

fully adiabatic cloud with a vertical extent of only 440 m (for a condensation rate corresponding to a cloud temperature of 283 K, which was used for all DYCOMS-II simulations). Radiative transfer simulations for the subadiabatic as well as the corresponding adiabatic cloud were performed. Subsequent retrievals on the simulated radiances for the two clouds confirm that the subadiabatic stratification of the actual clouds leads to the bias in LWP. It is caused by slight positive biases in both cloud optical thickness ($\tau = 42$ versus $\tau = 41$ for the equivalent adiabatic cloud) and effective radius (15.8 μm versus 15.4 μm). Note, that this deviation results from the subadiabatic LWC alone. Neither variations in CDNC nor the optical properties of the precipitation underneath contribute significantly to the bias (not shown).

4.3. Retrieving RWP

[23] The fundamental PMW observable with respect to liquid water is the transmittance or optical depth of the atmosphere (see, e.g., equations (5) and (10) by *Hilburn and Wentz* [2008]). Here we use the term A for optical depth consistent with the terminology of *Hilburn and Wentz* [2008] (who use the term "attenuation," hence "A"). This quantity can be restored from the available satellite observations using the formulae provided by *Hilburn and Wentz* [2008] and *Wentz and Spencer* [1998] as also pointed out and done by *Seethala and Horvath* [2010].

[24] Very similar to *Hilburn and Wentz* [2008] we can now write A as a sum of two different contributions:

$$A = \sigma_L \cdot LWP + \sigma_R \cdot RWP \tag{1}$$

where the mass extinction coefficient of liquid water σ_L is temperature-dependent but independent of LWP. The mass extinction coefficient of rain σ_R is a function of precipitation size distribution. This can be seen in Figure 5, where we plot σ_R for two different size distributions, namely a Marshall-Palmer size distribution of rain (henceforth "MP") and a drizzle size distribution according to *Wood* [2005b]. Both are plotted against rainwater content (RWC) and functional fits are provided as well. The MP fit agrees well with the fit provided by *Hilburn and Wentz* [2008] (their equation (17b)). Note that *Hilburn and Wentz* [2008] parameterize in terms of rain rate and volume extinction coefficient. In contrast, we parameterize in terms of RWC and mass extinction coefficient since we are interested in the RWP. RWC and RWP are assumed to be related via:

$$RWP = H_R \cdot RWC \tag{2}$$

with H_R being the rain column height (not to be confused with the cloud geometrical thickness for which we use H in this paper). The above equation is to say that the value of RWC is thought representative for the entire rain layer, again similar to the reasoning of *Hilburn and Wentz* [2008]. Our parameterization for the MP mass absorption coefficient is:

$$\sigma_{R,MP} = \alpha \left(\frac{RWP}{H_R} \right)^{\beta} \tag{3}$$

and for the W05 mass absorption coefficient:

$$\sigma_{R,MP} = a + b \cdot \frac{RWP}{H_R} \tag{4}$$

with the numerical values of the coefficients given in Figure 5. The latter fit ceases to fit well for RWC values higher than about 0.5 g/m^3 whereas the former holds up to values of about 1 g/m^3. With these equations we can now formally solve equation (1) for RWP for the two cases of a MP and W05 size distribution. This yields two different models for the retrieval of RWP:

$$RWP_{MP} = \left(\frac{A - \sigma_L \cdot LWP}{\alpha} \right)^{\frac{1}{\beta+1}} H_R^{\frac{\beta}{\beta+1}} \tag{5}$$

and for the W05 size distribution:

$$RWP_{W05} = -\frac{aH_R}{2b} + \sqrt{\left(\frac{aH_R}{2b} \right)^2 + \frac{H_R}{b}(A - \sigma_L \cdot LWP)} \tag{6}$$

RWP is thus a function of three unknowns, namely LWP, H_R, and A, where the latter one is the fundamental PMW observation. As pointed out earlier, up to this point we strictly follow what has been published earlier with the only exception that our particular form of the extinction coefficient is slightly different. For more details on the general PMW retrieval methodology the reader is referred to the work of *Hilburn and Wentz* [2008], *Petty* [1994a, 1994b], and *Wentz and Spencer* [1998].

[25] In order to solve the above equation, values for LWP and H_R need to be found. In our case we use LWP from VNIR observations. This provides another piece of independent physical information at the pixel level, and is different from PMW-only retrievals of rain rate. In contrast, PMW-only retrievals use what we refer to as a "climatological LWP/RWP partitioning" which is derived by fitting rain rate and/or rain frequency globally to other observations. This process is described nicely by *Hilburn and Wentz* [2008].

[26] The value of H_R is determined by *Hilburn and Wentz* [2008] as a function of sea surface temperature. In their work it is essentially associated with the height of the freezing level. In contrast, here we use the cloud top height derived from the infrared cloud top temperature, which is signifi-

cantly lower (and more realistic) than the freezing level at least for the type of warm clouds we are interested in.

[27] With these considerations we arrive at three different ways to derive RWP, which we term W05, MP, and DIFF:

[28] MP: PMW observations are used to derive A. VNIR observations are used to derive LWP. H_R is derived from cloud top temperature. With these three pieces of information equation (5) is used to solve for RWP.

[29] W05: Same as MP except that equation (6) is used corresponding to the W05 size distribution.

[30] DIFF: This method is very similar to MP. The only difference is that we do not use H_R derived from cloud top temperature but the original value used by *Hilburn and Wentz* [2008] which is representative for the height of the freezing level. We call this method DIFF because in this case RWP can be derived simply by subtracting the VNIR LWP from TWP as derived following *Seethala and Horvath* [2010]. This method is somewhat less realistic than MP in our case since it assumes the rain layer thickness to be too large (i.e., the freezing level is much higher than the actual cloud top for the clouds we are studying).

[31] In section 6 we will compare results of the different methods based on observations. For the modeling study described in Figure 4, Figure 4 (bottom) exemplarily compares the RWP (using the DIFF method) with the actual RWP of the stratiform cloud. Note, that random negative retrievals of RWP in precipitation-free cases are to be expected because of the noise imposed on the retrievals. In any actual retrieval it is important to keep negative values in order not to bias results positive when averaging. The aforementioned systematic positive bias in LWP (due to subadiabaticity) from VNIR of about 20 g/m^2 is small but not negligible compared to the maximum values of RWP of 104 g/m^2. The uncertainty about the liquid water content vertical profile will thus in any case affect the absolute accuracy of this type of retrieval. However, the explicit separation approach proposed here might still be extremely useful when inferring RWP (and also rain rate) from warm clouds since it circumvents the implicit assumptions made about LWP/RWP separation in PMW-only approaches [see, e.g., *O'Dell et al.*, 2008]. The proposed approach will in section 6 be tested with the observational data described in section 5.

5. Observational Data

5.1. Satellite Observations

[32] Satellite observations were available for one month (February 2009). Subsequently, we describe the different data.

5.2. Passive Microwave Observations

[33] Operational LWP retrievals from PMW from the Unified Microwave Ocean Retrieval Algorithm (UMORA) as applied to AMSR-E [*Hilburn and Wentz*, 2008; *Wentz*, 1997; *Wentz and Spencer*, 1998] were used. This algorithm uses five microwave channels in such a way that variations in sea surface temperature, total column water vapor, and surface wind speed have a minimal effect. The spatial resolution of the LWP product is about 14 × 11 km^2. Errors and uncertainties in LWP estimates are discussed by *O'Dell et al.* [2008]. The expected theoretical accuracy of the various products is discussed by F. J. Wentz and T. Meissner, in the Algorithm Theoretical Basis Document (ATBD): AMSR Ocean Algorithm, version 2, available at http://eospso.gsfc.nasa.gov/eos_homepage/for_scientists/atbd. AMSR-E data are available in HDF format from the National Snow and Ice Data Center (NSIDC). Level 2 data are separated in individual files that contain half-orbits of the retrieved products together with quality flags indicating retrieval accuracy as well as auxiliary information such as latitude, longitude, and observation geometry.

[34] As outlined earlier the separation between the PMW observation of TWP and LWP reported in the Ocean product is done based on global correlative statistics and might not be appropriate for individual cases. In order to obtain direct physical observations from the PMW, the LWP reported in the AMSR-E Ocean product were converted back to TWP by reverse engineering the method outlined by *Hilburn and Wentz* [2008] and *Wentz and Spencer* [1998]. For an overview of TWP versus LWP, the methodology, reverse engineering, and accuracy see the work of *O'Dell et al.* [2008] and in particular *Seethala and Horvath* [2010].

5.3. Visible/Near-Infrared Observations

[35] Coincident VNIR observations were available from EUMETSAT's Meteosat Second Generation (MSG) Spinning Enhanced Visible and Infrared Imager (SEVIRI), a 12 channel imaging instrument covering the spectral range between 0.6 and 13 μm [*Schmetz et al.*, 2002]. The retrievals of LWP from SEVIRI were performed with the Cloud Physical Properties (CPP) algorithm of the Satellite Application Facility on Climate Monitoring (CM-SAF) [*Roebeling, et al.*, 2006]. This algorithm retrieves cloud optical thickness, particle size and cloud phase simultaneously from visible (0.6 μm) and near-infrared (1.6 μm) reflectances and infrared (10.8 μm) brightness temperatures. Satellite observed visible and near-infrared reflectances are compared to look up tables (LUTs) of simulated reflectances of horizontally and vertically homogeneous water and ice clouds, generated with the Doubling Adding KNMI (DAK) radiative transfer model [*Stammes*, 2001]. DAK has been developed for monochromatic multiple scattering calculations at UV, visible and near infrared wavelengths in a plane-parallel cloudy atmosphere using the doubling-adding method. The retrieval of cloud phase is done simultaneously with the retrieval of cloud optical thickness and particle size. The phase "ice" is assigned to pixels for which the observed 0.6 μm and 1.6 μm reflectances correspond to simulated reflectances of ice clouds and the cloud top temperature is lower than 265 K. The remaining cloudy pixels are considered to represent water clouds. The retrievals are limited to satellite and solar viewing zenith angles smaller than 72°.

5.4. CloudSat Cloud Profiling Radar

[36] CloudSat radar observations collocated with AMSR-E and SEVIRI were available for the entire period. While only available on a narrow swath, these data provide an important reference for the occurrence of precipitation and are used wherever possible. CloudSat [*Stephens et al.*, 2002; *Stephens et al.*, 2008] carries the single-frequency, W-band (94 GHz) CPR [*Tanelli et al.*, 2008], and has provided global cloud and precipitation profiles since 2006. The CPR is a nonscanning, near-nadir pointing instrument with a mean spatial resolution

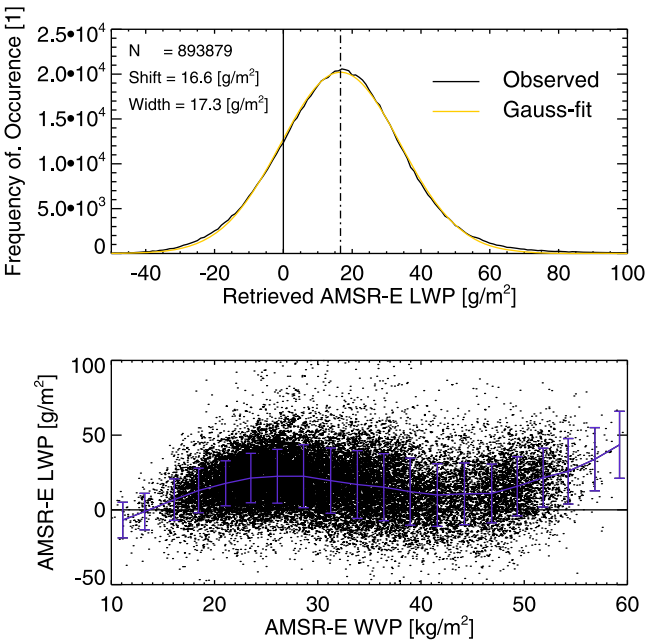

Figure 6. (top) Histogram of retrieved AMSR-E LWP for cloud-free observations. Cloud clearing was performed using SEVIRI VNIR observations. The solid curve shows the actual observations, and the yellow curve shows a fitted Gaussian distribution. (bottom) Retrieved cloud-free AMSR-E LWP as function of AMSR-E derived WVP. The curve gives the binned average and standard deviation; the dots are individual observations (about 10% of the individual observations are shown).

of ~1.5 km and a vertical range gate spacing of 500 m, although instrument oversampling enables 240 m data bins in the CloudSat data products. In this study only 2B-Geometric Profile (2B-GEOPROF) radar reflectivity profiles obtained from the CloudSat Data Processing Center are utilized. Further product documentation can be obtained from the CloudSat Data Processing Center.

5.5. Temporal and Spatial Matching of Different Observational Data Sets

[37] All data are collocated on a nearest-neighbor basis. The three different observation systems used in this study have different observation geometries and observation time. Since SEVIRI observes each scene every 15 min, the maximum time difference between SEVIRI and either AMSR-E or CloudSat is less than 7.5 min. The time difference between AMSR-E and CloudSat is in the order of less than two minutes since both are aligned within the A-train. Hence time differences are small and considered reasonable for this investigation.

[38] The differences in spatial resolution between AMSR-E and SEVIRI is accounted for by averaging 5 × 5 SEVIRI pixels to obtain roughly the same resolution as AMSR-E. Note that full convolution of SEVIRI to AMSR-E accounting for the near-Gaussian shape of the AMSR-E 36.5 GHz footprint is in principle feasible too, but considered unnecessary here. For details on convolution methodology, errors, and uncertainties see the work of *Bauer et al.* [1998], *Bennartz* [1999, 2000], *Greenwald* [2009], and *Greenwald et al.* [2007]. In order to minimize the impact of contamination with ice clouds in the subsequent data evaluation only those observations are used for which all individual 5 × 5 SEVIRI pixels were found to be either cloud-free or liquid water clouds as identified by the cloud mask, cloud top temperature, and cloud phase. Combined observations were also excluded if in any of the 5 × 5 SEVIRI pixels retrievals could not be performed. These measures effectively eliminate issues with unrealistic retrievals in broken cloud scenes at the cost of reducing the total data amount by about 20%.

6. Observation Results

6.1. Comparison of LWP/TWP Estimates Between SEVIRI and AMSR-E

[39] Before the RWP retrievals are studied, the consistency of the one-month combined PMW and VNIR data set is studied. Special emphasis is put on the comparison of VNIR and PMW LWP retrievals at the low end, defined as between cloud-free and LWP values up to about 150 g/m^2. In this range precipitation is still unlikely to occur. For those cases, ideally and on average, the two LWP retrievals should yield identical results.

6.2. Cloud-Free LWP Bias

[40] The studies by *Greenwald* [2009] and *Seethala and Horvath* [2010] suggest a (mostly) positive bias for AMSR-E LWP observations in cloud-free regions. *Greenwald* [2009] argues this bias can also be found in cloudy regions, so that AMSR-E observations are in total thought to overestimate LWP by about 20 g/m^2. Since in this study AMSR-E data are used as one input to derive RWP, the error statistics of LWP at the low end are of some importance. Figure 6 shows the histogram of cloud-cleared LWP values, i.e., AMSR-E retrievals of LWP for cases where the 5 × 5 VNIR observations all detect cloud-free ocean surface. The idea is that for an ideal retrieval, the distribution of retrieved LWP for cloud-free areas should be Gaussian and centered around zero, where the width of the Gaussian distribution is determine by the effects of random sensor noise on the retrieval. Cloud-free observations are therefore extremely useful to determine biases as well as retrieval uncertainties at the low end of the LWP spectrum. Indeed, the distribution of cloud-free LWP values in Figure 6 shows a near-Gaussian behavior with a comparably low standard deviation of 17.3 g/m^2. Very similar to the findings of *Greenwald* [2009] a mean positive bias of 16.6 g/m^2 is found, which depends on WVP (Figure 6, bottom). A regression of cloud-free LWP against WVP did not, however, show significant skill, because of the large scatter in the observations (see dots in Figure 6, bottom). The reason for this bias as well as for the correlation between LWP bias and WVP is unknown, but thought to be rooted in assumptions made in the retrieval process (e.g., water vapor absorption coefficient and temperature profile).

6.3. Cloudy Areas

[41] Figure 7 shows a comparison of retrieved SEVIRI (VNIR) LWP values with corresponding AMSR-E derived (PWM) LWP values. In addition, the same is shown for the PMW-derived TWP values (red curve). The bias found in the cloud-free observations can also be identified here, again,

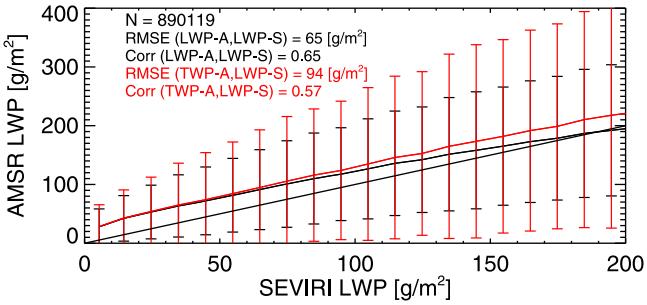

Figure 7. Comparison of SEVIRI-derived (VNIR) LWP with AMSR-E derived (PMW) LWP/TWP values. The black curve with errors bars shows the PMW LWP, and the red curve shows the TWP comparison. LWP-A: LWP from AMSR-E; LWP-S: LWP from SEVIRI; TWP-A: TWP from AMSR-E.

similar to the findings of *Greenwald* [2009]. It is interesting that the TWP comparisons (red curve) show a more consistent bias ranging all the way up to 200 g/m^2 whereas the bias in LWP reduces to about zero for VNIR LWP values above roughly 180 g/m^2. This seems to indicate that the separation of LWP and RWP done in the original PMW retrieval and described by *Hilburn and Wentz* [2008] compensated partly for the positive bias in the LWP retrievals by "pushing" more liquid water in the rain category. When results are converted back to the more physically direct TWP estimate (red curve), the bias remains also for higher LWP values. Clearly, more studies are needed in order to understand the reason for this bias. However, for the current paper this is only of relevance insofar as this bias will affect RWP estimates. On the basis of the results presented here, we will perform a first-order correction for the subsequent RWP estimates in that we subtract a constant value of 16.6 g/m^2 from the PMW TWP estimates.

6.4. Comparison of RWP With CloudSat CPR

[42] While the above considerations provide some initial insight into the noise characteristics, independent information on precipitation intensity can be obtained from the radar based on CloudSat. For a narrow track within each AMSR-E swath CloudSat's CPR provides 94 GHz radar observations. Figure 8 shows the retrieved RWP values as a function of maximum radar reflectivity in the observed column (starting three bins above the surface bin) for all data within the entire month. The color-coding corresponds to the three different assumptions in the RWP retrieval discussed above. Individual observations (black dots) are only plotted for the W05 assumption corresponding to the yellow line. For maximum radar reflectivity values lower than about −15 to −10 dBz RWP exhibits a flat behavior very close to zero with a slightly positively bias for all three retrievals. The low-end standard deviation of RWP for the precipitation-free cases based on CPR is about 80 g/m^2 for the DIFF assumption but significantly lower for physically more realistic W05 and MP (in the order of 30–40 g/m^2). This result is reassuring as it gives a good estimate of RWP retrievals at the low end (i.e., when no rain is present). Note, that outliers in RWP (e.g., RWP estimates beyond ±100 g/m^2 at around −28 dBz) also affect the standard deviation at the low end. It is likely that these outliers are associated with mismatches between the two instruments and/or other technical issues.

[43] For values above about −15 to −10 dBZ, the mean RWP starts to increase with increasing maximum reflectivity. These results are roughly consistent with the findings of *Suzuki and Stephens* [2008] who find collision/coalescence to occur at reflectivities higher than −10 dBz based on an analysis of coincident MODIS/CloudSat data. Maximum RWP values exceed 250 g/m^2 for W05 and 150 g/m^2 for MP, although it has to be noted that the data density above about +10 dBZ is quite low. The spread between W05 and MP gives a good measure for the uncertainty introduced by lack of knowledge about the raindroplet size distribution and the resulting difference in mass extinction coefficient, which manifests itself here as an uncertainty of about ±50% around the average value between W05 and MP. The issue of a particular choice and appropriateness of a certain size distribution will clearly have to be studied more in future work. Subsequently, we will only use results for W05 but associated uncertainties should be kept in mind.

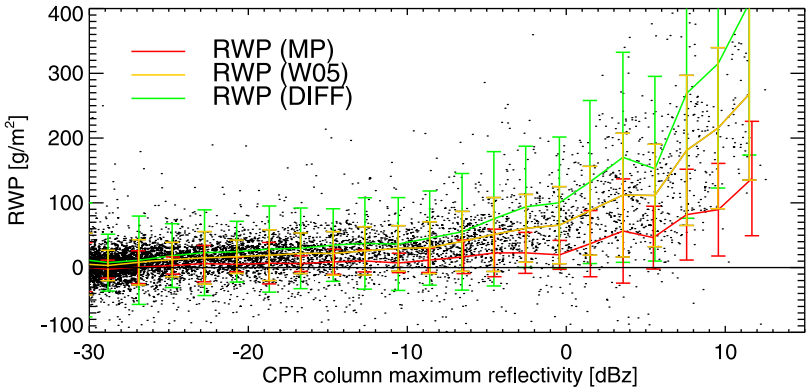

Figure 8. Rainwater path derived from AMSR-E/SEVIRI (8700 data points) as function of CloudSat CPR column maximum radar reflectivity. The three different curves show results for RWP retrievals if different assumptions about size distribution are made with the Marshall-Palmer size distribution (MP), *Wood* [2005b] (W05), and the simple difference between the reconstructed TWP from AMSR-E and the LWP from SEVIRI (DIFF). For details, see text. The curves show results binned in 2 dBz intervals. The error bars are the standard deviation in each interval.

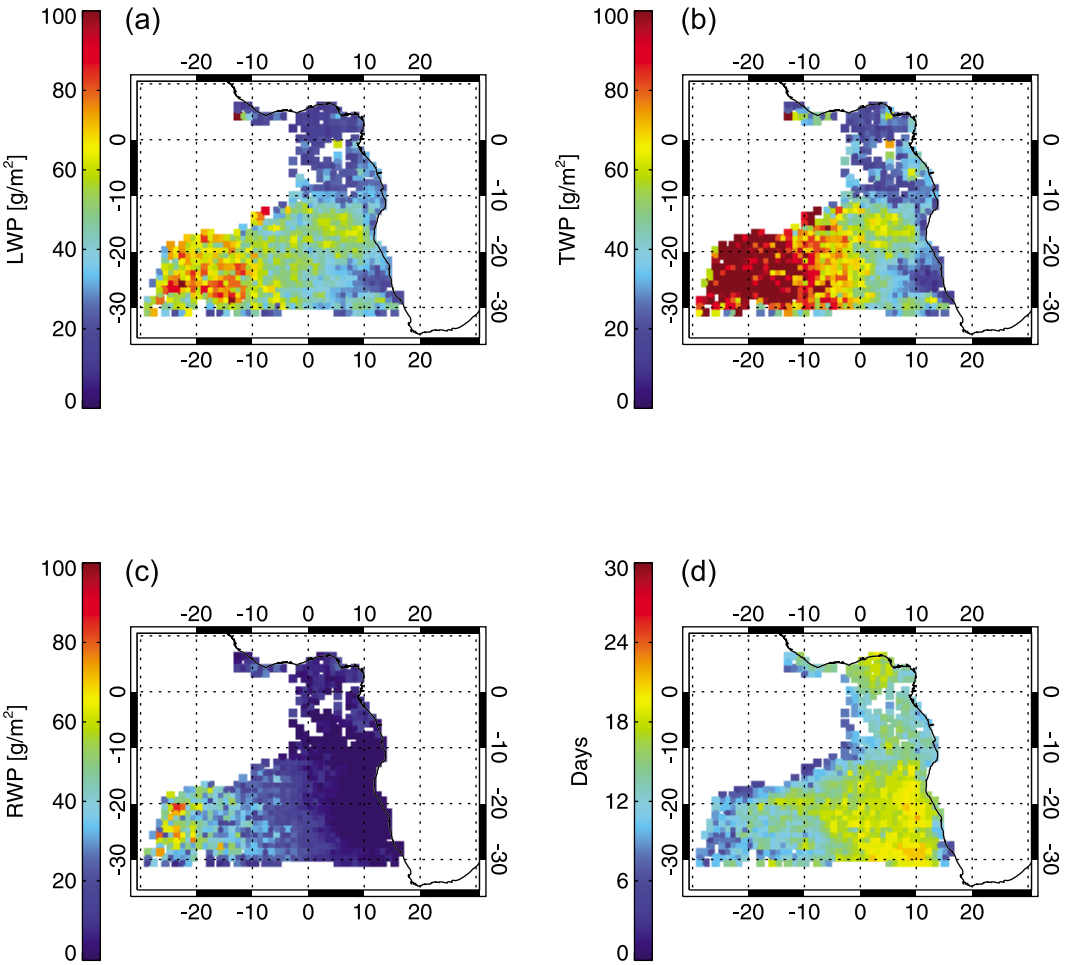

Figure 9. (a) Monthly mean SEVIRI LWP, (b) AMSR-E TWP, and (c) AMSR-E/SEVIRI RWP at 1 × 1 degree resolution. (d) The number of days with valid observations within the month for each 1 × 1 degree bin.

6.5. Rainwater Path

[44] Figure 9 shows monthly mean values for SEVIRI LWP, AMSR-E TWP, and SEVIRI/AMSR-E RWP for the investigation area. The area in the upper left quadrant of each image (around 10°S to 0°N and 20°W to 10°W) does not contain any valid data because of SEVIRI sunglint contamination for the particular overpass time of AMSR-E (Aqua equator crossing time around 1330 LST). SEVIRI LWP is highest around 25°S/15°W with another maximum for a large patch near 15°S/5°E corresponding to the center of the stratocumulus area. Recall that here we are only concerned with warm clouds, i.e., clouds not involving ice phase. Thus values of LWP, TWP, and RWP shown here do not include liquid water associated with any form of deep convective clouds or frontal systems. North of 10°S SEVIRI LWP decreases mostly because warm cloud fraction significantly decreases (not shown). AMSR-E TWP in the stratocumulus area is high too but increases sharply from near the coast of southern Africa toward the west of the investigation area. SEVIRI/AMSR-E RWP shown here is derived using the above W05 size distribution and plotted in Figure 9c. It shows a very clear transition from east to west with near-zero RWP near the coast and values around 60 g/m^2 near 20°S/20°W. The stratocumulus area, which can clearly be identified both in the SEVIRI LWP and AMSR-E TWP, shows very small values for RWP. Figure 10 shows monthly mean values of cloud droplet number concentration (N), geometrical thickness (H), $1/N$ and H^3/N. As outlined above, the latter two are of particular importance since theoretical and experimental studies suggest that precipitation intensity scales with H^3/N, thus is proportional to $1/N$. Indeed the spatial distribution of $1/N$ and H^3/N resembles the spatial distribution of RWP quite well. Figure 11 shows scatterplots of the $1/N$ and H^3/N against RWP together with regression fits. Both quantities are exceptionally well correlated with RWP with an explained variance of 0.52 and 0.69, respectively, corresponding to correlation coefficients of 0.72 and 0.83, respectively. Other variables, such as in-cloud and grid box-averaged LWP show a somewhat lower explained variance of around 0.45 (not shown).

7. Conclusions

[45] In this paper we explore the capabilities of combined passive microwave and visible/near infrared observations to obtain rainwater path. A simple conceptual cloud model together with radiative transfer simulations is used to exploit the information content of the different observations types and study the retrieval in a highly idealized theoretical

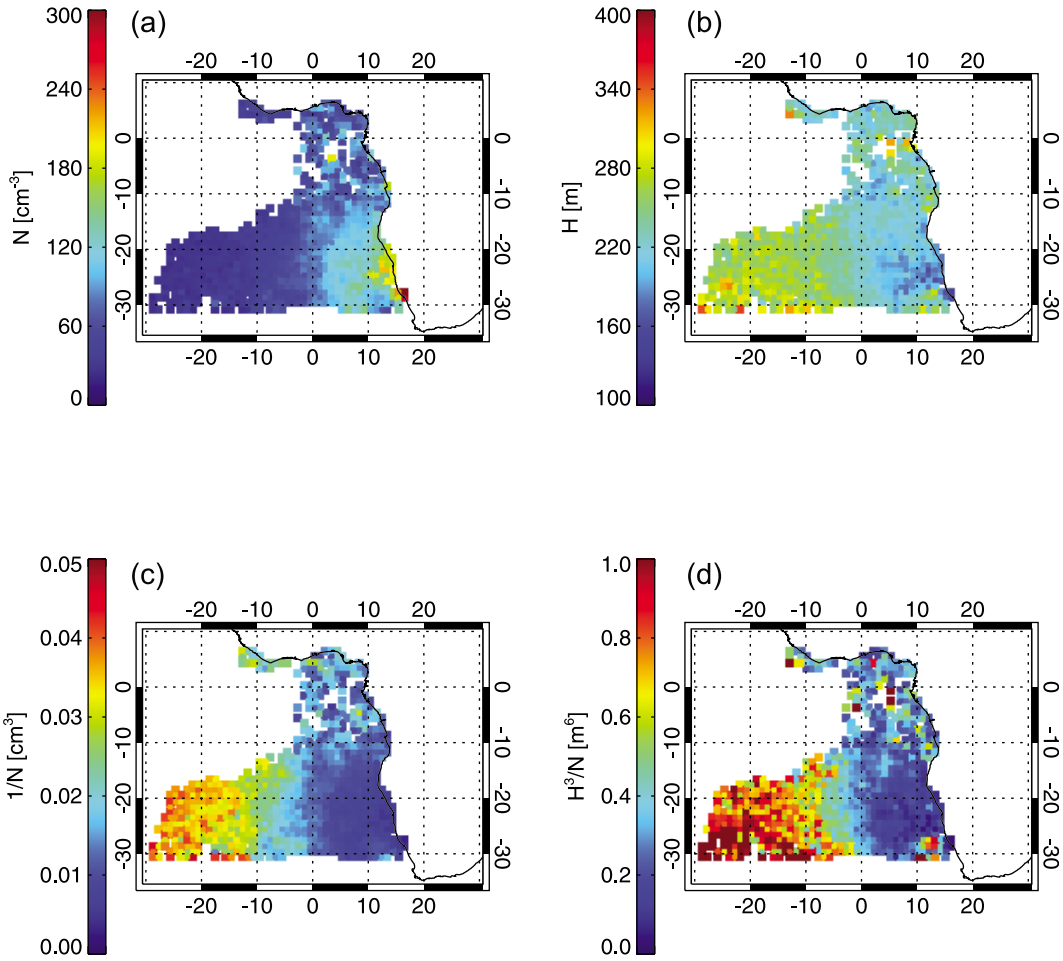

Figure 10. (a) Monthly mean values of cloud droplet number concentration, (b) cloud geometrical thickness, (c) 1/N, and (d) H^3/N from SEVIRI at 1 × 1 degree resolution.

framework. We then apply the method using one month of combined passive microwave and visible/near-infrared observations. The method is evaluated against CloudSat radar reflectivities. The combination of passive microwave and visible/near-infrared observations proposed in this paper will possibly lead to new methods of detecting and quantifying light, warm rain. The methods will circumvent critical issues related to the climatological separation of rainwater and cloud liquid water used in current passive microwave only algorithms.

[46] Comparing rainwater path estimates to other retrieved quantities, such as liquid water path and cloud droplet number concentration it is found that the estimates of rainwater path are highly correlated with the inverse of cloud droplet number concentration. This finding highlights the effect of cloud microphysics on precipitation generation and is consistent with other empirical and theoretical studies.

[47] Various caveats remain. In particular, three effects were investigated here. First, the vertical stratification of cloud liquid water has been confirmed to affect the relation between liquid water path and the optical properties of clouds derived from visible/near-infrared observations. This effect might lead to potential biases in liquid water retrieval not only in the framework of rainwater path retrievals but also for liquid water path retrievals from visible/near-infrared observations. Second, biases were confirmed to exist in retrievals of liquid (and total) water path from PMW observations. Both effects are tightly coupled to the respective initial retrievals. While the second effect was accounted for using an ad hoc bias correction, the first effect has not been taken into account in the rainwater path retrievals performed here. Indeed, the comparison with CloudSat reveals a slight positive bias for rainwater path retrievals for nonprecipitating clouds. Comparisons with CloudSat radar reflectivities might in future studies be used to tune the rainwater path retrievals accordingly, or to test algorithm improvements. Third, the particular choice of a raindroplet size distribution plays a significant role in determining the absolute value of rainwater path and contributes significantly to the uncertainty in rainwater path retrieval.

[48] Another main restriction of the current study lies in the selection of the observations used. In order to isolate the effect of rainwater path the data have been screened so that broken cloud scenes were largely excluded. This screening helps to avoid issues with currently poorly understood potentially anomalous retrievals of, e.g., very high effective radii from visible/near-infrared observations that frequently occur in broken cloud regions. While this is not

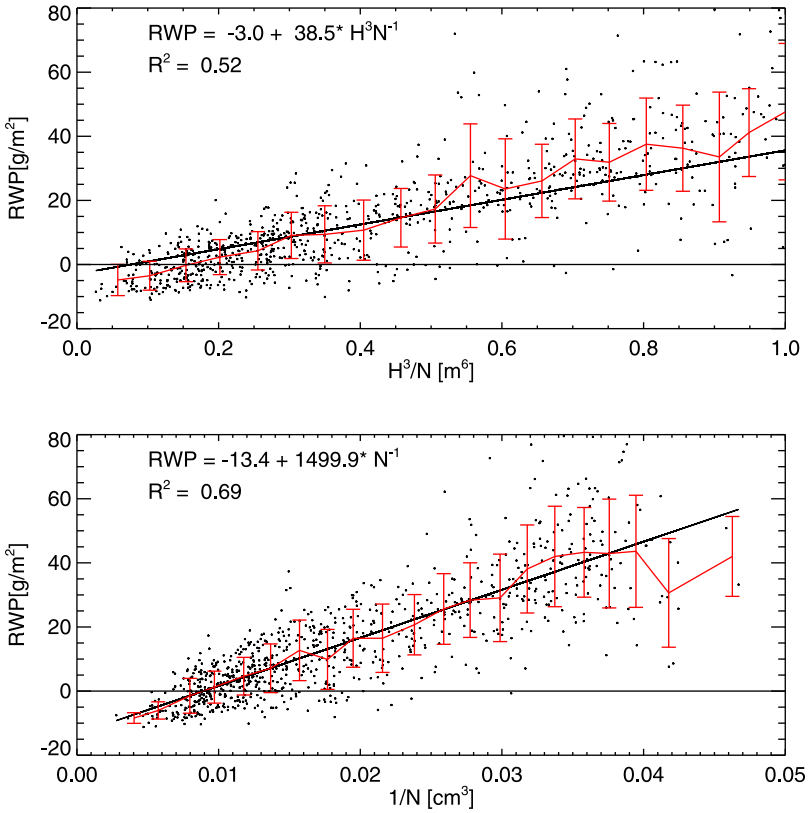

Figure 11. Rainwater path derived from AMSR-E/SEVIRI at 1 × 1 degree resolution as function of (top) H^3/N and (bottom) 1/N. The dots are individual monthly mean values. The red curve shows results binned in 0.1 m^6 intervals of H^3/N and 0.002 cm^3 intervals of 1/N, respectively. The error bars are the standard deviation in each bin. The black line is the regression fit with parameters given in the insets and units as shown on the axis labels.

the focus of the current study, it should be kept in mind that this restrictive data selection will potentially bias climatologies especially in areas where broken clouds occur frequently.

[49] Additionally, the results presented shed some light on biases reported between passive microwave and visible/near-infrared estimates of liquid water path. These will need to be accounted for and the results presented in various earlier studies potentially need to be re-evaluated including effects of rainwater in the passive microwave and the effects of stratification of cloud liquid water in the visible/near-infrared.

[50] It appears that it would be possible to derive surface or cloud base rain rate based on the initial results presented here. This would require a more realistic modeling of warm rain processes, including raindroplet size distribution, evaporation underneath cloud base, and a subsequent retrieval of precipitation rate based on cloud top height and rainwater path. All these items are deferred to later studies.

Appendix A: Conceptual Cloud Model

A1. Model Description

[51] The model's four prognostic variables are cloud water content (q_c), rainwater content (q_R), cloud droplet number concentration (N_c), and rain number concentration (N_R). The prognostic equations are:

$$\frac{\partial q_c}{\partial t} + w_{AIR}\frac{\partial q_c}{\partial z} = -P_{AUTO} - P_{ACC} + P_{COND} - P_{ENTR} \quad \text{(A1)}$$

$$\frac{\partial q_R}{\partial t} + (w_{RAIN} - w_{AIR})\frac{\partial q_R}{\partial z} = P_{AUTO} + P_{ACC} \quad \text{(A2)}$$

$$\frac{\partial N_c}{\partial t} + w_{AIR}\frac{\partial N_c}{\partial z} = P_{N,ACT} - \frac{P_{AUTO} + P_{ACC} + P_{ENTR}}{q_c} \quad \text{(A3)}$$

$$\frac{\partial N_R}{\partial t} + (w_{RAIN} - w_{AIR})\frac{\partial N_R}{\partial z} = \frac{P_{AUTO}}{\frac{4}{3}\pi\rho_L r_{R,0}^3} \quad \text{(A4)}$$

The symbols are explained in Table A1 and the terms in the prognostic equations are explained in detail in below. Source terms on the right-hand side of the equations are shown with a positive sign and sink terms with a negative sign. The model is set up with a vertical resolution of 1 m and the time step is chosen accordingly as $dt = 1/w_{AIR}$.

A2. Autoconversion and Accretion

[52] While various formulations in particular for the autoconversion rate exist, *Wood* [2000] shows that the auto-

Table A1. Symbols and Terms Used Throughout This Paper

Symbol	Explanation	Unit
q_c, q_R	Cloud (rain) water content	kg/m^3
N_C, N_R	Cloud (rain) droplet number	m^{-3}
w_{AIR}, w_{RAIN}	Updraft velocity, rain fall velocity	m/s
ρ_L	Liquid water density	kg/m^3
P_{ACC}	Accretion production	kg/(m^3 s)
P_{AUTO}	Autoconversion production	kg/(m^3 s)
P_{COND}	Condensation production	kg/(m^3 s)
P_{ENTR}	Entrainment production	kg/(m^3 s)
$P_{N,ACT}$	Production of cloud droplets at activation	1/(m^3 s)
w_{ENTR}	Entrainment velocity	m/s
c_w	Condensation rate	kg/m^4
$r_{R,0}$	Precipitation rate for autoconversion[a] (20 μm)	μm
N	Cloud droplet number concentration at activation[a]	cm^{-3}
H	Cloud geometrical thickness	m
H_R	Rain column height	m
r_V	Cloud volume radius[a]	μm
r_e	Cloud effective radius[a]	μm
$\sigma_{L,R}$	Mass absorption coefficient of cloud (L) or rain (R)	m^2/kg
A	Microwave optical thickness due to liquid and rain	N.D.
τ	Cloud optical thickness	N.D.
LWP	Cloud liquid water path[a]	g/m^2
PMW	Passive Microwave	
RWC	Rainwater content	g/m^3
RWP	Rainwater path[a]	g/m^2
TWP	Total liquid water path (LWP + RWP)[a]	g/m^2
VNIR	Visible/Near-infrared	
WVP	Water Vapor Path	kg/m^2

[a]Values are given in non-SI units throughout the paper.

conversion scheme by *Khairoutdinov and Kogan* [2000], hereafter termed KK, provides good results when compared to aircraft observations using a simple steady state cloud model accounting for autoconversion and accretion. On the basis of comparisons of aircraft observations with a Large Eddy Simulation (LES) model, *Geoffroy et al.* [2008] comes to the same conclusion. This parameterization of autoconversion and accretion is therefore used as a basis for the current publication as well:

$$P_{AUTO} = -\alpha N_c{}^{\beta} q_c^{\gamma} \tag{A5}$$

$$P_{ACC} = 67(q_R q_c)^{1.15} \tag{A6}$$

where q_c is the cloud water content, and q_r is the rainwater content. The values for the constants in equation (A5) for KK are $\alpha = 1350$; $\beta = -1.79$; $\gamma = 2.47$ with cloud droplet number concentration N given in [cm^{-3}], q_c given in [kg/m^3] and the autoconversion rate given in [kg/m^3/s]. For a compilation of different autoconversion schemes see, for example, the work of *Wood* [2005b]. Note, that for simplicity throughout this investigation no distinction is made between water content given in [kg/m^3] and mixing ratio in [kg/kg], thus the air density is assumed to be of unity. The resulting error for boundary layer clouds is small compared to the wide spread of different autoconversion rates and other uncertainties. Throughout this paper a minimum cloud liquid water threshold for instantaneous autoconversion of 0.25×10^{-3} kg/m^3 has been applied. If the cloud liquid water content is below this value, the autoconversion rate is assumed to be zero. This value obviously significantly affects the instantaneous autoconversion. It does not have a significant impact on the considerations below about effective autoconversion rates, since most of the precipitation production is much more efficient in the thicker parts of the clouds, when a distribution of cloud liquid water is assumed.

A3. Condensation Production

[53] Condensation production is calculated as a source of cloud liquid water above cloud base while the cloud is still growing. Condensation production is calculated using a fixed temperature-based condensation rate, so that a cloud without entrainment and precipitation generation would exhibit a linear vertical profile of liquid water content. Throughout this paper, the condensation rate has been fixed at $c_w = 3.5E - 6$ [kg/m^4], so that condensation production is $P_{COND} = w_{AIR} \cdot c_w$. The condensation rate is zero outside of the cloud boundaries, i.e., below cloud base and above cloud top.

A4. Activation of Cloud Droplets

[54] Cloud droplets are activated only at cloud base. The air passing from below through cloud base will be assigned an initial cloud droplet number concentration. After the cloud has reached its maximum extent, the updraft is switched off, and no additional activation occurs.

A5. Entrainment

[55] Characteristically for a horizontally homogeneous stratocumulus cloud, entrainment of dry air is only allowed from cloud top but not laterally. The dry air at cloud top is allowed to mix downward via a fixed entrainment velocity. Throughout the cloud the entrainment production term, which is a sink of cloud water, is proportional to minus the entrainment velocity times the vertical derivative of the deviation of the liquid content from its adiabatic maximum value:

$$P_{ENTR} = -w_{ENTR} \frac{\partial \left(q_{c,ADIABATIC} - q_c\right)}{\partial z} \tag{A7}$$

The entrainment velocity for the stratocumulus cases was set to 0.7 cm/s, which is at the high end of the observational results reported by *Faloona et al.* [2005].

[56] **Acknowledgments.** Steven Platnick and Graeme Stephens are gratefully acknowledged for triggering this research by asking the right questions. This work was carried out during a visiting scientist stay of the first author at EUMETSAT who are gratefully acknowledged for their hospitality and support of this work. This research was also partly funded under NASA grant NNX08AF92G and by the German Weather Service (DWD) via EUMETSAT's Satellite Application Facility on Climate Monitoring (CM-SAF).

References

Bauer, P., L. Schanz, R. Bennartz, and P. Schlussel (1998), Outlook for combined TMI-VIRS algorithms for TRMM: Lessons from the PIP and AIP projects, *J. Atmos. Sci.*, *55*, 1714–1729, doi:10.1175/1520-0469(1998)055<1714:OFCTVA>2.0.CO;2.

Bennartz, R. (1999), On the use of SSM/I measurements in coastal regions, *J. Atmos. Oceanic Technol.*, *16*, 417–431, doi:10.1175/1520-0426(1999)016<0417:OTUOSI>2.0.CO;2.

Bennartz, R. (2000), Optimal convolution of AMSU-B to AMSU-A, *J. Atmos. Oceanic Technol.* , *17*, 1215–1225, doi:10.1175/1520-0426(2000)017<1215:OCOABT>2.0.CO;2.

Bennartz, R. (2007), Global assessment of marine boundary layer cloud droplet number concentration from satellite, *J. Geophys. Res.*, *112*, D02201, doi:10.1029/2006JD007547.

Borg, L. A., and R. Bennartz (2007), Vertical structure of stratiform marine boundary layer clouds and its impact on cloud albedo, *Geophys. Res. Lett.*, *34*, L05807, doi:10.1029/2006GL028713.

Brenguier, J. L., H. Pawlowska, L. Schüller, R. Preusker, J. Fischer, and Y. Fouquart (2000), Radiative properties of boundary layer clouds: Droplet effective radius versus number concentration, *J. Atmos. Sci.*, *57*, 803–821, doi:10.1175/1520-0469(2000)057<0803:RPOBLC>2.0.CO;2.

Comstock, K. K., R. Wood, S. E. Yuter, and C. S. Bretherton (2004), Reflectivity and rain rate in and below drizzling stratocumulus, *Q. J. R. Meteorol. Soc.*, *130*, 2891–2918, doi:10.1256/qj.03.187.

Deblonde, G., and S. English (2001), Evaluation of the FASTEM-2 fast microwave oceanic surface emissivity model, *Tech. Proc. ITSC-XI*, Budapest, 67–78.

Faloona, I., D. H. Lenschow, T. Campos, B. Stevens, M. van Zanten, B. Blomquist, D. Thornton, A. Bandy, and H. Gerber (2005), Observations of entrainment in eastern Pacific marine stratocumulus using three conserved scalars, *J. Atmos. Sci.*, *62*, 3268–3285, doi:10.1175/JAS3541.1.

Geoffroy, O., J. L. Brenguier, and I. Sandu (2008), Relationship between drizzle rate, liquid water path and droplet concentration at the scale of a stratocumulus cloud system, *Atmos. Chem. Phys.*, *8*, 4641–4654, doi:10.5194/acp-8-4641-2008.

Greenwald, T. J. (2009), A 2 year comparison of AMSR-E and MODIS cloud liquid water path observations, *Geophys. Res. Lett.*, *36*, L20805, doi:10.1029/2009GL040394.

Greenwald, T. J., T. S. L'Ecuyer, and S. A. Christopher (2007), Evaluating specific error characteristics of microwave-derived cloud liquid water products, *Geophys. Res. Lett.*, *34*, L22807, doi:10.1029/2007GL031180.

Heidinger, A. K., C. O'Dell, R. Bennartz, and T. Greenwald (2006), The successive-order-of-interaction radiative transfer model. Part I: Model development, *J. Appl. Meteorol. Climatol.*, *45*, 1388–1402, doi:10.1175/JAM2387.1.

Hilburn, K., and F. J. Wentz (2008), Intercalibrated passive microwave rain products from the unified microwave ocean retrieval algorithm (UMORA), *J. Appl. Meteorol. Climatol.*, *47*, 778–794, doi:10.1175/2007JAMC1635.1.

Horvath, A., and R. Davies (2007), Comparison of microwave and optical cloud water path estimates from TMI, MODIS, and MISR, *J. Geophys. Res.*, *112*, D01202, doi:10.1029/2006JD007101.

Khairoutdinov, M., and Y. Kogan (2000), A new cloud physics parameterization in a large-eddy simulation model of marine stratocumulus, *Mon. Weather Rev.*, *128*, 229–243, doi:10.1175/1520-0493(2000)128<0229:ANCPPI>2.0.CO;2.

Kostinski, A. B. (2008), Drizzle rates versus cloud depths for marine stratocumuli, *Environ. Res. Lett.*, *3*, 045019, doi:10.1088/1748-9326/3/4/045019.

Kummerow, C., Y. Hong, W. S. Olson, S. Yang, R. F. Adler, J. McCollum, R. Ferraro, G. Petty, D. B. Shin, and T. T. Wilheit (2001), The evolution of the Goddard profiling algorithm (GPROF) for rainfall estimation from passive microwave sensors, *J. Appl. Meteorol.*, *40*, 1801–1820, doi:10.1175/1520-0450(2001)040<1801:TEOTGP>2.0.CO;2.

Liebe, H. J., G. A. Hufford, and T. Manabe (1991), A model for the complex permittivity of water at frequencies below 1 Thz, *Int. J. Infrared Millimeter Waves*, *12*, 659–675, doi:10.1007/BF01008897.

Martin, G. M., D. W. Johnson, and A. Spice (1994), The measurement and parameterization of effective radius of droplets in warm stratocumulus clouds, *J. Atmos. Sci.*, *51*, 1823–1842, doi:10.1175/1520-0469(1994)051<1823:TMAPOE>2.0.CO;2.

Nakajima, T., and M. D. King (1990), Determination of the optical-thickness and effective particle radius of clouds from reflected solar-radiation measurements. 1. Theory, *J. Atmos. Sci.*, *47*, 1878–1893, doi:10.1175/1520-0469(1990)047<1878:DOTOTA>2.0.CO;2.

O'Dell, C. W., A. K. Heidinger, T. Greenwald, P. Bauer, and R. Bennartz (2006), The successive-order-of-interaction radiative transfer model. Part II: Model performance and applications, *J. Appl. Meteorol. Climatol.*, *45*, 1403–1413, doi:10.1175/JAM2409.1.

O'Dell, C. W., F. J. Wentz, and R. Bennartz (2008), Cloud liquid water path from satellite-based passive microwave observations: A new climatology over the global oceans, *J. Clim.*, *21*, 1721–1739, doi:10.1175/2007JCLI1958.1.

Pawlowska, H., and J. L. Brenguier (2000), Microphysical properties of stratocumulus clouds during ACE-2, *Tellus, Ser. B*, *52*, 868–887, doi:10.1034/j.1600-0889.2000.00076.x.

Pawlowska, H., and J. L. Brenguier (2003), An observational study of drizzle formation in stratocumulus clouds for general circulation model (GCM) parameterizations, *J. Geophys. Res.*, *108*(D15), 8630, doi:10.1029/2002JD002679.

Petty, G. W. (1994a), Physical retrievals of over-ocean rain rate from multichannel microwave imagery. 1. Theoretical characteristics of normalized polarization and scattering indexes, *Meteorol. Atmos. Phys.*, *54*, 79–99, doi:10.1007/BF01030053.

Petty, G. W. (1994b), Physical retrievals of over-ocean rain rate from multichannel microwave imagery. 2. Algorithm implementation, *Meteorol. Atmos. Phys.*, *54*, 101–121, doi:10.1007/BF01030054.

Roebeling, R., and I. Holleman (2009), SEVIRI rainfall retrieval and validation using weather radar observations, *J. Geophys. Res.*, *114*, D21202, doi:10.1029/2009JD012102.

Roebeling, R. A., A. J. Feijt, and P. Stammes (2006), Cloud property retrievals for climate monitoring: Implications of differences between Spinning Enhanced Visible and Infrared Imager (SEVIRI) on METEOSAT-8 and Advanced Very High Resolution Radiometer (AVHRR) on NOAA-17, *J. Geophys. Res.*, *111*, D20210, doi:10.1029/2005JD006990.

Rosenkranz, P. W. (1999), Correction to "Water vapor microwave continuum absorption: A comparison of measurements and models" by Philip W. Rosenkranz, *Radio Sci.*, *34*, 1025–1025, doi:10.1029/1999RS900020.

Schmetz, J., P. Pili, S. Tjemkes, D. Just, J. Kerkmann, S. Rota, and A. Ratier (2002), An introduction to Meteosat Second Generation (MSG), *Bull. Am. Meteorol. Soc.*, *83*, 977–992, doi:10.1175/1520-0477(2002)083<0977:AITMSG>2.3.CO;2.

Schüller, L., J. L. Brenguier, and H. Pawlowska (2003), Retrieval of microphysical, geometrical, and radiative properties of marine stratocumulus from remote sensing, *J. Geophys. Res.*, *108*(D15), 8631, doi:10.1029/2002JD002680.

Seethala, C., and A. Horvath (2010), Global assessment of AMSR-E and MODIS cloud liquid water path retrievals in warm oceanic clouds, *J. Geophys. Res.*, *115*, D13202, doi:10.1029/2009JD012662.

Shao, H., and G. Liu (2004), Detecting drizzle in marine warm clouds using combined visible, infrared and microwave satellite data, *J. Geophys. Res.*, *109*, D07205, doi:10.1029/2003JD004286.

Stammes, P. (2001), Spectral radiance modeling in the UV-Visible range, in *IRS 2000: Current Problems in Atmospheric Radiation, Proceedings of the International Radiation Symposium, St. Peterberg, Russia, 24-29 July 2000*, edited by W. L. Smith and Y. M. Timofeyev, pp. 385–388, A. Deepak, Hampton, Va.

Stephens, G. L., et al. (2002), The CloudSat mission and the A-Train: A new dimension of space-based observations of clouds and precipitation, *Bull. Am. Meteorol. Soc.*, *83*, 1771–1790.

Stephens, G. L., et al. (2008), CloudSat mission: Performance and early science after the first year of operation, *J. Geophys. Res.*, *113*, D00A18, doi:10.1029/2008JD009982.

Stevens, B., et al. (2003), Dynamics and chemistry of marine stratocumulus—DYCOMS-II, *Bull. Am. Meteorol. Soc.*, *84*, 579–593, doi:10.1175/BAMS-84-5-579.

Suzuki, K., and G. L. Stephens (2008), Global identification of warm cloud microphysical processes with combined use of A-Train observations, *Geophys. Res. Lett.*, *35*, L08805, doi:10.1029/2008GL033590.

Tanelli, S., S. L. Durden, E. Im, K. S. Pak, D. G. Reinke, P. Partain, J. M. Haynes, and R. T. Marchand (2008), CloudSat's cloud profiling radar after two years in orbit: Performance, calibration, and processing, *IEEE Trans. Geosci. Remote Sens.*, *46*, 3560–3573, doi:10.1109/TGRS.2008.2002030.

van Zanten, M. C., B. Stevens, G. Vali, and D. H. Lenschow (2005), Observations of drizzle in nocturnal marine stratocumulus, *J. Atmos. Sci.*, *62*, 88–106, doi:10.1175/JAS-3355.1.

Wentz, F. J. (1997), A well-calibrated ocean algorithm for special sensor microwave/imager, *J. Geophys. Res.*, *102*, 8703–8718, doi:10.1029/96JC01751.

Wentz, F. J., and R. W. Spencer (1998), SSM/I rain retrievals within a unified all-weather ocean algorithm, *J. Atmos. Sci.*, *55*, 1613–1627, doi:10.1175/1520-0469(1998)055<1613:SIRRWA>2.0.CO;2.

Wilcox, E. M., Harshvardhan, and S. Platnick (2009), Estimate of the impact of absorbing aerosol over cloud on the MODIS retrievals of cloud optical thickness and effective radius using two independent retrievals of liquid water path, *J. Geophys. Res.*, *114*, D05210, doi:10.1029/2008JD010589.

Wood, R. (2000), The validation of drizzle parametrizations using aircraft data, paper presented at 13th International Conference on Clouds and Precipitation, Reno, Nev., 14–18 August 2000.

Wood, R. (2005a), Drizzle in stratiform boundary layer clouds. Part 1: Vertical and horizontal structure, *J. Atmos. Sci.*, *62*, 3011–3033, doi:10.1175/JAS3529.1.

Wood, R. (2005b), Drizzle in stratiform boundary layer clouds. Part II: Microphysical aspects, *J. Atmos. Sci.*, *62*, 3034–3050, doi:10.1175/JAS3530.1.

Wood, R., and D. L. Hartmann (2006), Spatial variability of liquid water path in marine low cloud: The importance of mesoscale cellular convection, *J. Clim.*, *19*, 1748–1764, doi:10.1175/JCLI3702.1.

Wood, R., T. Kubar, and D. L. Hartmann (2009), Understanding the importance of microphysics and macrophysics for warm rain in marine low clouds: Part II. Heuristic models of rain formation, *J. Atmos. Sci.*, *66*, 2973–2990.

R. Bennartz, Atmospheric and Oceanic Sciences, University of Wisconsin-Madison, 1225 W. Dayton St., Madison, WI 53706, USA. (bennartz@aos.wisc.edu)

P. Watts, EUMETSAT, Eumesat-Allee 1, D-64295 Darmstadt, Germany.

J. F. Meirink and R. Roebeling, KNMI, Wilhelminalaan 10, NL-3732 GK De Bilt, Netherlands.